Turbulent solutal convection and surface patterning in solid dissolution

Timothy S. Sullivan,[1,2] Yuanming Liu,[2] and Robert E. Ecke[2]
[1]*Department of Physics, Kenyon College, Gambier, Ohio 43022*
[2]*MST Division and Center for Nonlinear Studies, Los Alamos National Laboratory, Los Alamos, New Mexico 87545*
(Received 31 July 1995)

We describe experiments in which crystals of NaCl, KBr, and KCl are dissolved from below by aqueous solutions containing concentrations of the respective salts from zero concentration to near saturation. The solution near the solid-liquid interface is gravitationally unstable, producing turbulent hydrodynamic motion similar to thermal convection from a single surface cooled from above. The coupling of the fluid flow with the solid dissolution produces irregular patterns at the solid-liquid interface with a distribution of horizontal length scales. The dissolution mass flux and the pattern length scales are compared with a turbulent boundary layer model. Remarkable agreement is found, showing that the fluid motion controls both the dissolution rate and the interface patterning. [S1063-651X(96)06007-2]

PACS number(s): 47.27.−i, 47.20.Hw, 47.20.Bp

I. INTRODUCTION

In this paper we describe experiments in which crystals of NaCl, KBr, and KCl are dissolved in aqueous solutions of the respective salts. The experiments are arranged such that only a lower, horizontal surface is exposed to the solution; see Fig. 1. In this arrangement, a fluid layer with a higher concentration of salt is formed at the solid-liquid interface as the crystal dissolves. This fluid is more dense than the body of the liquid and (in the cases we consider) is gravitationally unstable and produces turbulent convective flow. We find that this convective flow controls the rate of dissolution of the solid. We report rates of dissolution for the three salts as a function of the concentration of the salt in the solution. We compare these results with a turbulent boundary layer model and find excellent agreement.

In addition, the solid-liquid interface does not remain flat as the salt dissolves. We present video micrographs and one- and two-dimensional profiles of these surfaces to characterize the resulting irregular pattern. A characteristic length scale of the pattern, determined using two independent methods that give values in good agreement, scaled with dissolution rate, as predicted from a linear stability analysis of the turbulent boundary layer model. This implies that the surface patterning is also controlled by the fluid motion.

This system has both intrinsic and practical interest. A recent proposal for fast etching of photoresists employs buoyancy-enhanced dissolution [1] as does a proposal for a recent technique in liquid-phase epitaxy [2]. Material transport by convection plays an important role in crystal growth and morphology [3–7]. In crystal growth, however, convection competes with other instabilities in shaping the solid-liquid interface [3,4]. By examining the process of dissolution, the effects of convection alone are isolated. As we discuss in detail below, there is a close analogy between convection driven by concentration gradients and convection driven by thermal gradients. Turbulent thermal convection is a very active area of research with recent advances in understanding the role of the boundary layer and its instability in determining heat transport [8–14]. Studies of solutal convection may provide additional insight into this process. For example, it provides a convenient way to achieve very high Rayleigh numbers (defined below). Dissolution in this geometry also presents a particularly well-defined experimental system for studying the coupling of a turbulent fluid flow with a moving boundary. Its simplicity should make it amenable to theoretical analysis.

The analogy between mass transport by convection and heat transport by convection, presented below in Sec. II, is frequently cited in textbooks on heat and mass transfer [15], but few experimental tests have been reported. So-called ''classical'' theories of thermal convection predict that the heat transport should scale as the $\frac{1}{3}$ power of the Rayleigh number at high Rayleigh number. Recent precision experiments [8–10] and theory [9,11] show that the heat transport scales as the $\frac{2}{7}$ power of the Rayleigh number at least in the Rayleigh-Bénard geometry where one has a heated bottom plate and a cooled top plate. Scaling for the single surface problem studied here has not been reexamined in light of these recent results. The scaling of dissolution rates has been reported by Goldstein, Sparrow, and Jones [16], who studied turbulent convection produced by the sublimation of naphthelene sheets in air. They explicitly invoked the analogy with thermal convection and cited the scaling results they obtained as evidence for the same scaling as in thermal convection. They worked at lower values of the Rayleigh number than the present experiments and did not report any pattern appearing on the naphthalene surface. Kerr [17] made quantitative measurements of dissolution rates of ice roofs in isopropanol solutions and ice floors in salt water solutions. He found that dissolution rates scaled as expected from classical turbulence theory and made qualitative observations of interface patterning. Fang and Hellawell [18] observed surface patterning in the dissolution of ice in brine solutions and of tin in liquid lead-tin alloys.

Although not completely analogous to dissolution, there are some closely related systems that have been studied. Interfacial patterning has been observed in systems with strong temperature effects: melting produced by turbulent solutal convection [19,20] and fluid flow coupled to a freezing-melting interface [21]. More relevant to our experiments are those that involve natural convection and horizontal solid-

liquid interfaces. A thermal convection experiment near the onset of convection, in which the upper surface is below the freezing point of the liquid, produces a solid-liquid interface with a modulation corresponding to the wavelength of the convection rolls produced by the unstable temperature gradient [22–24]. Although complicated by the density maximum at 4 °C, patterning of the surface of ice being melted from below has been reported [25,26]. Experiments on the melting of a frozen layer of low density by an overlaying warm liquid of higher density have been performed both for the case where the frozen material is miscible [27] and for the case where it is immiscible [28,29] in the liquid. In the miscible case [27], a range of Rayleigh numbers was found where the Nusselt number scaled as expected for the classical theory of thermal convection, but at high Rayleigh number the Nusselt number scaled with a much larger power (≈ 1) of the Rayleigh number than that observed in thermal convection. No explanation was offered for this behavior. In the immiscible case [28,29], good agreement was found by treating the layer of melt as Rayleigh-Taylor unstable. None of these experiments, however, are very close to pure dissolution as the rate of melting is determined by the flow of heat to the interface, not by the fluid motion itself.

Another closely related experimental system involves mass transfer in electrodeposition [30]. Electrodeposition of copper on an upper horizontal surface of copper generates a gravitationally unstable layer of electrolyte near the surface producing convective flow. The rate of deposition is controlled by the rate at which the flow brings fresh electrolyte near the surface. Experiments [31,32] have shown that the rate of electrodeposition scales as one would expect by analogy to thermal convection. Surface patterning was not reported, however.

The difference between the classical $\frac{1}{3}$ scaling and the recently discovered $\frac{2}{7}$ scaling is small and it is difficult to differentiate between them without the precise measurement of heat transport and the large range of Rayleigh numbers available in the experiments of [8–10]. None of the experiments mentioned above, nor ours described below, have the precision necessary to decide between the two alternatives. Further, the single-surface geometry in many of the experiments and in the experiments reported here has not been analyzed from the perspective of determining corrections to classical scaling. For example, the nature of the recirculating flow is different here. Thus we compare our results to the classical theory because, in that model, the heat flux is independent of vertical length scale for which there is no natural choice for a single boundary.

We will interpret our results using a model of a turbulent boundary layer described below in Sec. II. This model, based on the work of Howard, in the context of thermal convection [33], who extended earlier work by Malkus [34] and Priestly [35], predicts the classical scaling relation between heat transport and Rayleigh number. Howard considered the development of a gravitationally unstable fluid layer next to the horizontal, constant temperature boundaries of the fluid as heat was added or extracted from the fluid. This boundary layer grows thicker as heat flows into or out of the fluid until the layer becomes unstable and injects plumes into the body of the fluid. A simplifying assumption [33], that the layer is quiescent on average with a thickness δ governed by this instability, predicts a great deal and will explain much of our mass transport data. Foster [36] performed a linear stability analysis of the evolving boundary layer and predicted the horizontal wavelengths of the unstable modes. We will compare a characteristic length scale of our patterned interfaces with Foster's results.

Our paper is organized as follows. First, we present in Sec. II the theoretical formulation of the mass dissolution problem and describe the boundary-layer model for turbulent dissolution. We make a close analogy with thermal convection in our discussion. In Sec. III we describe the experimental apparatus and data acquisition procedures. The dissolution-rate data and surface-profile measurements are presented in Sec. IV and discussed and compared with theoretical predictions in Sec. V. Finally, we present our conclusions in Sec. VI.

II. THEORY

A. Solutal convection

Let us look at how one can make an analogy between a convection-dominated dissolution process and Rayleigh-Bénard convection. At the interface between a solid and a solvent capable of dissolving the solid, atoms are released into the solvent and (in the absence of fluid flow) diffuse away from the interface by a process obeying Fick's law

$$\vec{j} = -\rho D \vec{\nabla} c, \tag{1}$$

where $\vec{j}$ is the current of solute atoms, ρ is the density of the solution, D is the mass diffusivity of the solute atoms in the solvent, $c(\vec{r})$ is the solute concentration field measured as mass of solute per mass of solution, and $\vec{r}$ represents a position in the fluid. Generally, the dissolution process has a heat of solution associated with it and heat must be supplied to or extracted from the interface for the process to continue. In principle, either solutal or thermal diffusion could regulate the interface motion. We consider the case where solutal diffusion dominates. This will most often be the case because the thermal diffusivity κ of the material is typically much higher than its mass diffusivity (i.e., the material has a high Lewis number, which is the ratio of thermal to mass diffusivity) and because heat is supplied from many directions in the apparatus whereas mass transport is limited to the liquid-solid interface [37]. Another potentially competitive mass transfer process is the diffusion of liquid atoms into the solid material. This solid-state diffusion is negligible, however, because it is extremely slow for most materials. In the absence of convection, then, the interface motion is controlled by the rate of diffusion of the solid solute into the solution.

The concentration at the interface c_i is taken to be the saturated concentration of the solute in the solvent c_{sat}. Lommel and Chalmers [38] studied dissolution of lead in tin with diffusion alone and with vigorous stirring. When the fluid layer was gravitationally stable, the rate of dissolution was consistent with diffusion controlled by a saturated-solution boundary condition at the solid-liquid interface. When the fluid was stirred, however, the concentration at the interface could fall below the saturation concentration. Although natural convection could depress c_i, our results are consistent

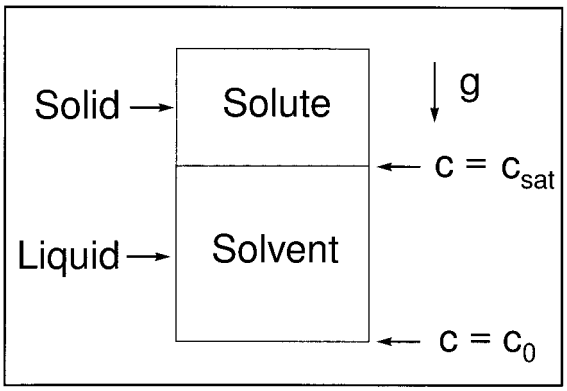

FIG. 1. Schematic diagram of dissolution geometry. c denotes the concentration of solute dissolved in the solvent, with c_{sat} the saturated concentration and c_0 the concentration far from the interface. The direction of the (uniform) gravitational field is shown.

with the hypothesis that $c_i = c_{\mathrm{sat}}$. The boundary condition $c_i = c_{\mathrm{sat}}$ is analogous to a constant temperature boundary condition in the Rayleigh-Bénard problem.

In the Rayleigh-Bénard problem, one completes the description with equations for the conservation of mass, energy, and momentum. In the solutal convection problem one has an additional equation expressing conservation of mass of solute

$$\frac{\partial(\rho c)}{\partial t} + \vec{\nabla}\cdot(\rho c\vec{u}) = \vec{\nabla}\cdot(\rho D\vec{\nabla}c), \tag{2}$$

which is completely analogous to the conservation of energy equation in thermal convection.

To simplify further, we invoke the Boussinesq approximation [39], which consists of several assumptions. First, one assumes that the properties of the fluid (the specific heat C, κ, the viscosity ν, and D) are constant over the range of temperature (and, here, concentration) existing in the fluid. The viscous heating term and the PdV term are neglected in the energy equation, the latter as a result of assuming that density changes are only a result of thermal or solutal expansion

$$\Delta\rho = (\rho - \rho_0) = \rho_0[-\alpha(T - T_0) + \beta(c - c_0)], \tag{3}$$

where ρ_0 is the density at some reference value of $T = T_0$ and $c = c_0$, α is the thermal expansion coefficient, and β is the solutal expansion coefficient. For positive β buoyancy-driven convection is produced for the geometry of Fig. 1. If β is negative, then convection occurs when the fluid layer lies above the solid rather than below. Finally, one assumes that the only place $\Delta\rho$ is important is in the gravitational force term in the Navier-Stokes equation. All other references to the density are replaced with ρ_0.

In the experiments reported here, the Boussinesq approximation is not always well satisfied. In the extreme case of KBr dissolving into fresh water, over the range from the saturated concentration at the interface to the fresh water in the bulk, the fluid viscosity varies by 23%, the mass diffusivity by 23%, and the density by 27%. For turbulent thermal convection, non-Boussinesq (NB) effects were studied for the Rayleigh-Bénard problem, but only from the perspective of asymmetry between the upper and lower boundaries [40]. The major effect in our case is the modification of the concentration profile in the boundary layer from the linear profile assumed in the boundary layer theory. A simulation of the diffusion equation with a temperature-dependent mass diffusion coefficient shows that for a relative change in D of about 25%, the concentration profile differs from the linear one by at most 6%. A corresponding change of about 6% in δ would result from this correction. This small effect on the scaling at the highest dissolution rates is within the scatter of the data. From these estimates and from the lack of quantitative differences in scaling in the experiments for highly NB conditions, we conclude that NB effects are of secondary importance here and ignore them in further discussion. Theoretical investigation of these corrections would certainly be welcomed.

For the typical dissolution process that we studied, the coupling between the temperature field and the equation of motion can be neglected because the density change owing to concentration variations will be large compared to that from temperature variations. For example, in the case of KBr dissolving into fresh water we estimate the temperature of the interface to be about 0.3 °C below ambient. Since the thermal expansion coefficient of water is 2×10^{-4} K^{-1}, this yields $\Delta\rho/\rho \approx 6\times10^{-5}$ owing to thermal effects. Since $\Delta\rho/\rho \approx 0.3$ from concentration variations, the bouyancy induced by temperature variations can be ignored.

Since the equation for the concentration field and the temperature field are of the same form, there is a direct analogy between the solutal convection problem and the Rayleigh-Bénard problem of thermal convection. In thermal convection [39] the equations are made dimensionless by normalizing length by the height of the fluid layer d, time by the viscous diffusion time $\tau_\nu = d^2/\nu$, and temperature by the temperature difference across the fluid layer ΔT. The equations are written in terms of two nondimensional parameters, the Rayleigh number $R = g(\alpha\Delta T)d^3/\nu\kappa$ and the Prandtl number $\mathrm{Pr} = \nu/\kappa$.

For the solutal convection problem, the equation for the temperature field does not couple to the equation of motion. Then with the same choice of scales for length and time as in the thermal problem, the resulting solutal equations can be written in terms of two nondimensional numbers analogous to the thermal convection case. The first is the mass transport Rayleigh number $R_m = g(\beta\Delta c)d^3/\nu D$ and the second is the Schmidt number $S_c = \nu/D$.

Thus we see a direct analogy between thermal convection and solutal convection within the stated assumptions. This analogy can be useful. The qualitative nature of the type of flow to be expected (steady, turbulent, etc.) is well mapped out for thermal convection and provides a guide for what to expect in the solutal convection case.

B. Turbulent boundary layer

To describe turbulent thermal convection, Howard [33] postulated the existence of a boundary layer at the solid-fluid interface whose thickness δ just satisfied the condition for the onset of Rayleigh-Bénard convection. Heat was assumed to be transported across this layer by thermal diffusion. With the same assumption for the solutal convection problem, the

mass transport current density j is related to the boundary layer thickness δ by the assumption of diffusive transport across the layer

$$\delta = \frac{\rho D \Delta c}{j}. \tag{4}$$

Accepting the simple marginal stability hypothesis [34], one can relate δ to an effective critical Rayleigh number for the boundary layer

$$R_c = \frac{g\beta \Delta c \delta^3}{\nu D} \approx \frac{g \Delta \rho \delta^3}{\nu \rho D}, \tag{5}$$

where the fluid parameters are the mean values over the boundary layer depth. To obtain R_c from experimental data, we define a length scale $\delta_0 = (\nu D/g)^{1/3}$ so that

$$\delta/\delta_0 = \left(\frac{R_c}{\Delta \rho/\rho} \right)^{1/3}. \tag{6}$$

A power law fit of δ/δ_0 versus $\Delta\rho/\rho$ allows a test of the predicted $-\frac{1}{3}$ exponent and yields values for R_c.

Howard also described the dynamics of the boundary layer as consisting of a thickening of the boundary layer as heat diffused into the fluid, followed by buoyant instability and separation from the solid-fluid interface, and finally by the formation of a new layer by thermal diffusion. Howard worked out a characteristic period τ for this dynamic boundary layer ($\tau = \delta^2/\pi\kappa$). Foster applied some of his earlier work [36] to obtain a linear stability and weakly nonlinear analysis of this dynamic boundary layer [41]. In particular, he worked out the wavelength of the fastest growing mode in the direction parallel to the solid-fluid interface. In the absence of a more complete theory, this lateral length scale is a logical starting point for understanding the surface patterning observed in our experiments. In the case of a sudden application of a fixed temperature difference (here a fixed $\Delta\rho/\rho$), Foster found that an initial step concentration profile evolved into an error function profile that became hydrodynamically unstable to perturbations of wavelength:

$$\lambda = 51(D\nu\rho/g\Delta\rho)^{1/3} \tag{7}$$

for large values of the Schmidt number. Using Eq. (5), one can rewrite this as

$$\lambda = 51(R_c)^{-1/3}\delta. \tag{8}$$

III. EXPERIMENT

The crystals used in the experiments were NaCl, KBr, and KCl spectrophotometer window blanks [42]. Each had a nominal size of $19\times38\times6$ mm^3. During different trials, we exposed each of the three possible faces to the solution. To confine the dissolution process to only the chosen face, we epoxied the crystal into a fixture that exposed only that one face to the solution. The tank containing the solution and within which the dissolution took place was constructed of clear Plexiglas and was about 13 cm wide by 26 cm long by 16 cm tall. The solution in the dissolution tank was temperature regulated to about 0.1 °C by a temperature controlled water bath. The solutions were prepared with a precision of 0.1% by adding a measured mass of technical grade NaCl, KBr, or KCl to the known mass of water and solute in the bath. Preparing the solution with a desired concentration meant adding salt to the tank. This caused a large change in the solution temperature owing to the heat of dissolution of the salt. We waited until the solution temperature returned to within 2 °C of 20 °C before starting the dissolution of a crystal. Our absolute knowledge of the solution concentration was degraded by about 2% by possible evaporation of water from the tank between runs.

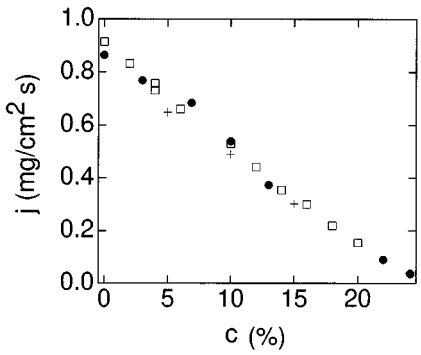

FIG. 2. j vs c for NaCl with exposed face A (+), B (●), and C (□).

For convenience, the three possible faces of the crystal are designated A (19×38 mm^2), B (38×6 mm^2), and C (19×6 mm^2). In exposures of face A, the surface was sanded and polished to near optical smoothness and the crystal was immersed in the solution and allowed to dissolve until its mass was about half the starting value. It was then removed and the surface blown dry with compressed gas. These crystals were never reexposed to solution. Video micrographs and surface profiles of these surfaces are presented below. To conserve crystals, exposures of faces B and C typically involved multiple immersions in different concentration solutions with one-quarter (for type B) to one-sixth (for type C) of the crystal dissolved during each exposure. For the first immersion the surface was sanded and polished as for surface A, but since the surface was subsequently inaccessible inside its protective fixture, polishing was impossible and subsequent exposures had an initial surface that resulted from the previous exposure. The mass flux j is the time rate of change of the mass of the crystal per unit area exposed to the solution. Figure 2 is a plot of the mass flux versus solution concentration for NaCl. Different symbols designate which face was exposed to the solution. Within the scatter of the data, there is no systematic variation of the mass flux with which face was exposed to the solution. This is somewhat remarkable. When surfaces B or C are exposed, convection occurs in a rather narrow (6-mm) slot formed by the cavity remaining after the crystal dissolves some distance, whereas there are no lateral constraints for surface A. In reporting on some convection experiments [15,16] the authors use a lateral length scale in defining the Rayleigh number. For our case, the lateral size appears to be irrelevant. (Some of the observed scatter in the raw data can be attributed to differences in the solution temperature for the different trials. Some of that is accounted for in the comparison with the model expectations in Sec. V.) In addition, the ini-

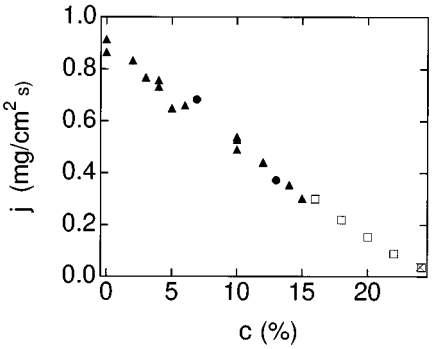

FIG. 3. j vs c for NaCl with fluid heights: 4.6 cm (●), 7.6 cm (□), 9.0–9.5 cm (▲), and 10 cm (×).

tial surface configurations for faces B and C were quite variable, as described above. The lack of noticable variation of j with which face is exposed thus shows that surface configuration is not a strong influence on the dissolution rate.

The fixture containing the crystal was supported at a measured, fixed height above the bottom of the dissolution tank by an adjustable stand. Figure 3 plots the same data as Fig. 2, except that the different symbols now indicate different starting heights of the interface above the bottom of the dissolution tank. For the purposes of this plot, the data are divided into four groups: low (4.6 cm), medium (7.6 cm), high (between 9.0 and 9.5 cm), and highest (10 cm). Again, there does not appear to be a systematic variation of the mass flux with height of the fluid layer. Since our results are insensitive to variations in height, we analyze our data in a way not involving the height. In other words, our experiments appear to be well approximated by a single surface exposed to a semi-infinite fluid reservoir.

As mentioned above, the solid-liquid interface did not remain flat as the crystal dissolved. To characterize the surface pattern we used two techniques. The first was to shine light through the crystal from below and observe the pattern in video micrographs. Selected images are shown in Fig. 4. This gives a measure of the lateral length scale, but reveals nothing quantitative about variations in the surface height. To obtain that information we constructed a simple profilometer. The profilometer consisted of two major parts: a computer controlled, horizontal XY translation stage [43], which was capable of high-precision positioning (resolution 50 nm, repeatability 100 nm, and accuracy 1 μm), and a sharp tip (with a radius of curvature of about 0.125 mm) coupled to a fixed linear voltage displacement transducer (LVDT) [44] for measurement of vertical displacement. We mounted the tip on a pivoted rod with an adjustable counterbalance. We could thus adjust the tip pressure on the surface to achieve good tracking with minimum pressure to avoid scratching the surface. Owing to lateral freedom in the pivot, some artifacts were observed on steep slopes of surfaces. This degrades the overall resolution of the profilometer relative to the translation stage. We estimate our lateral reproducibility was typically ± 20 μm. We varied the tip radius and found no significant difference in the low-frequency power spectrum of our surface profiles. We checked for surface damage by making two measurements on one crystal surface. The two measurements yielded almost identical power spectra (except at very high wave number). The signal from the

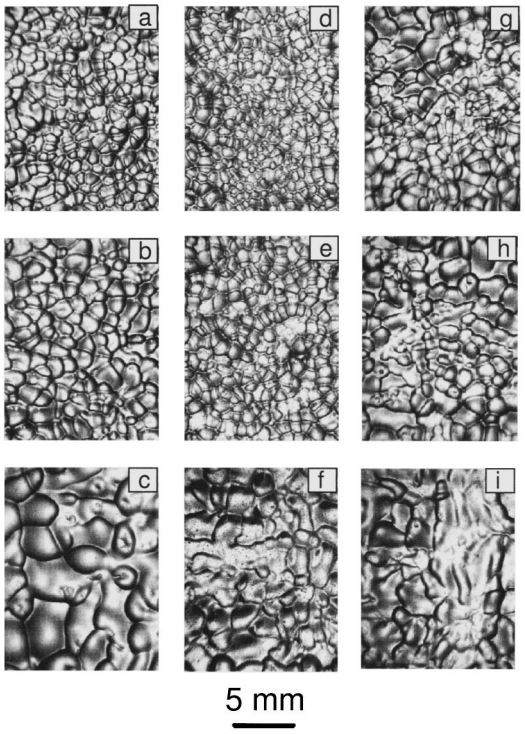

FIG. 4. Video micrographs of surface morphology for salt surfaces exposed to solutions of NaCl (left): a (0%), b (10%), c (24%); KBr (center): d (0%), e (10.7%), f (34%); KCl (right): g (0%), h (12.1%), i (20.5%).

LVDT was read with a multimeter and recorded by computer. The LVDT calibration is such that 1 mV represented a displacement of 1.5 μm. Using this system, we measured profiles of surfaces of each of the three types of salts exposed to solutions of various concentrations. Each exposed crystal surface was of type A (38×19 mm^2). The central portion with an area 20×10 mm^2 was scanned with a resolution of 512×256. Each profile measurement took about 12 h.

IV. RESULTS

A. Dissolution

Dissolution rates were determined by two techniques. In the first, the crystal was backlit by diffuse light and the dissolution recorded on video tape. The interface position (at the midpoint of the longest side exposed to the fluid) was digitized and plots of interface position versus time were constructed. An example is shown in Fig. 5 for a sample of NaCl dissolving in fresh water. Under all conditions observed, these plots were linear within our resolution, indicating that the dissolution rate was constant over the time of the trial. The dissolution mass flux was then calculated from the slopes of these plots, the known density of the salt, and the measured area of the interface. In the second method, the dissolution mass flux was calculated from the mass difference of the fixture before and after the dissolution, the time the fixture remained in the solution, and the measured area of the exposed surface. The two methods gave consistent results.

Figure 6 plots the observed dissolution mass flux as a function of concentration for NaCl, KBr, and KCl. The data

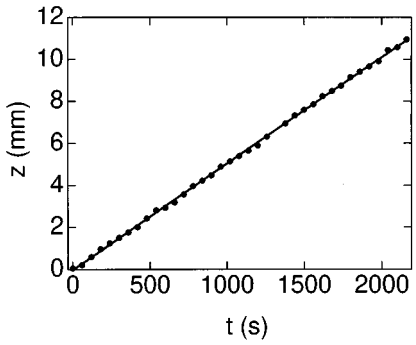

FIG. 5. Interface position z vs t for a NaCl crystal dissolving in fresh water ($c=0$).

are tabulated in Tables I–III. The driving force for solutal convection is $\Delta\rho/\rho=\beta\Delta c$, where $\Delta c=c_{\mathrm{sat}}-c$. Therefore, the dissolution mass flux was highest when the crystals were exposed to fresh water and decreased to zero as the solution concentration approached the saturated concentration of the salt. The dissolution rate of KBr was higher than that of NaCl or KCl because both c_{sat} and β are about 50% higher for KBr than they are in NaCl or KCl.

To compare with the model, the fluid properties (density, viscosity, diffusivity, and saturated concentration) must be determined as a function of concentration and temperature (at least near the nominal operating temperature of 20 °C). For NaCl, the density was taken from a published power series [45] and the saturated concentration (a very weak function of temperature [46]) was taken to be constant at 26.38%. The viscosity was numerically interpolated from the data for the viscosity as a function of concentration at 20 °C [47]. The temperature dependence of the viscosity was accounted for by using linear interpolation with data [48] at a few concentrations at temperatures of 10 °C and 30 °C. The diffusivity as a function of concentration at 25 °C [49] is adjusted for temperature using the Stokes-Einstein relation and the viscosity determined as above. For KBr, the density as a function of concentration seems only available [47] at 20 °C, so no temperature correction was possible. The saturated concentration is determined by linear interpolation of the data near 20 °C [46]. The viscosity of KBr is determined by linear interpolation between the data at 20 °C [47] and the data at 25 °C [50]. The diffusivity is determined in the same way and from the same source as for NaCl. For KCl the density, saturated concentration, and viscosity are given as a

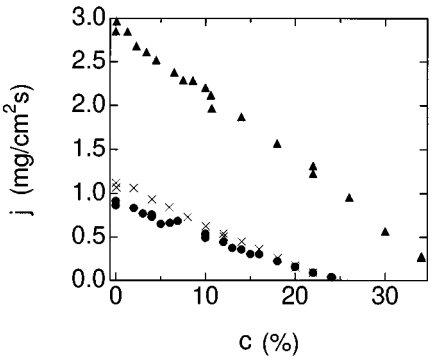

FIG. 6. j vs c for NaCl (●), KBr (▲), and KCl (×).

TABLE I. $\Delta\rho/\rho$, j, δ, and δ/δ_0 for NaCl for given c and T.

T (°C)	c (wt. %)	$\Delta\rho/\rho$	j (mg/cm^2 s)	δ (10^{-2} mm)	δ/δ_0
20.2	0.0	0.179	0.864	5.39	9.00
20.0	0.0	0.179	0.914	5.11	8.52
20.0	3.0	0.157	0.769	5.21	8.73
20.3	4.0	0.150	0.731	5.25	8.82
20.4	4.0	0.150	0.758	5.07	8.51
20.1	5.0	0.143	0.648	5.68	9.51
20.5	6.0	0.136	0.660	5.36	8.97
22.0	6.9	0.130	0.684	4.96	8.37
22.6	10.0	0.108	0.539	5.52	9.28
23.0	10.0	0.108	0.529	5.48	9.25
20.5	10.0	0.114	0.490	5.80	9.63
21.8	12.0	0.0940	0.441	5.82	9.69
21.5	13.0	0.0872	0.373	6.44	10.67
21.7	14.0	0.0804	0.355	6.30	10.4
20.2	15.0	0.0736	0.302	6.83	11.2
21.6	16.0	0.0693	0.300	6.23	10.2
20.7	18.0	0.0537	0.220	7.00	11.3
20.4	20.0	0.0406	0.155	7.67	12.3
20.7	22.0	0.0277	0.0888	9.30	14.8
20.6	24.0	0.0150	0.0377	12.1	18.9
20.6	24.1	0.0143	0.0363	12.0	18.8
20.8	24.1	0.0143	0.0353	12.33	19.3

functions of concentration and temperature in Ref. [51]. The diffusivity is again determined as for NaCl.

B. Surface patterns

Figure 4 shows video micrographs of type-*A* surfaces of NaCl, KBr, and KCl after exposure to solutions of concen-

TABLE II. $\Delta\rho/\rho$, j, δ, and δ/δ_0 for KBr for given c and T.

T (°C)	c (wt. %)	$\Delta\rho/\rho$	j (mg/cm^2 s)	δ (10^{-2} mm)	δ/δ_0
21.3	0.0	0.318	2.85	3.79	6.44
21.1	0.1	0.318	2.97	3.53	6.04
20.9	1.3	0.309	2.85	3.50	6.05
20.3	2.3	0.301	2.68	3.62	6.27
19.8	3.4	0.293	2.61	3.61	6.26
19.6	4.5	0.286	2.52	3.66	6.36
19.9	6.5	0.271	2.38	3.71	6.46
19.8	7.5	0.264	2.29	3.73	6.50
19.7	8.6	0.256	2.29	3.64	6.36
19.3	10.6	0.241	2.12	3.72	6.51
19.8	10.7	0.240	1.97	4.01	7.01
19.5	14.0	0.216	1.87	3.81	6.68
20.4	18.0	0.185	1.57	3.98	6.98
20.3	22.0	0.153	1.32	4.24	7.44
19.8	22.0	0.153	1.23	4.24	7.44
20.1	26.0	0.122	0.954	4.32	7.57
19.3	30.0	0.0878	0.567	5.23	9.14
19.5	34.0	0.0535	0.278	6.26	10.9
19.9	34.0	0.0535	0.263	6.73	11.7

TABLE III. $\Delta\rho/\rho$, j, δ, and δ/δ_0 for KCl for given c and T.

T (°C)	c (wt. %)	$\Delta\rho/\rho$	j (mg/cm^2 s)	δ (10^{-2} mm)	δ/δ_0
20.5	0.0	0.161	1.12	4.58	8.11
20.5	0.1	0.161	1.07	4.70	8.35
20.2	2.0	0.149	1.06	4.37	7.79
20.1	4.0	0.136	0.931	4.56	8.14
20.3	6.0	0.123	0.841	4.69	8.37
20.0	8.0	0.111	0.728	4.87	8.69
20.1	10.0	0.0985	0.622	5.14	9.15
20.7	12.0	0.0858	0.539	5.40	9.59
20.7	12.1	0.0849	0.504	5.32	9.65
20.8	14.0	0.0729	0.448	5.64	10.0
20.8	16.0	0.0602	0.361	5.93	10.5
20.8	18.1	0.0476	0.256	6.63	11.7
20.4	20.0	0.0349	0.174	7.20	12.7
20.7	20.1	0.0342	0.148	8.64	15.3
20.8	22.0	0.0228	0.0884	9.50	16.7

trations as given in the figure caption. In each case approximately half of the 6 mm depth of the crystal was dissolved. One observes that the surfaces are not flat but consist of broad concavities (white areas) separated by relatively narrow ridges (dark regions). All micrographs are of the same magnification. Each column of micrographs corresponds to one material. In each column, the solution concentration increases and the dissolution rate decreases as you go down the column. So one can see that the characteristic size of the concavities is a decreasing function of the dissolution rate. This is consistent (see Sec. V below) with the fact that the smaller the convective forcing the larger the boundary layer thickness predicted by the model. A characteristic length scale ($l=\sqrt{A/N}$) was obtained from the images by counting the number of depressions N in a given area A of the sample. A corresponding wave number ($k=2\pi/l$) as a function of concentration is plotted in Fig. 7(a). Another method for obtaining k is described next.

In Fig. 8 we show surface profiles and corresponding contour plots determined with our profilometer of the surface of crystals of NaCl exposed to solutions with concentrations of 0%, 15%, and 24%. In order to better compare the surface features among the different images, the horizontal scale has been magnified for the images at 0% and 15% concentration. One can see the irregular nature of the surface patterning. Figure 9 shows representative profiles consisting of 20-mm scans across the center of the NaCl surfaces for solutions with five different concentrations. The height variation is of order a few tenths of millimeter with a characteristic wavelength that increases with solution concentration.

To get a more quantitative picture of the lateral length scales, we analyzed the surface profiles with two-dimensional (2D) Fourier transform methods. The power spectrum of the 2D Fourier transform is defined as

$$S(\vec{k})=\left|\int\int h(x,y)\exp[i(k_x x+k_y y)]dx\,dy\right|^2, \qquad (9)$$

where k_x and k_y are the wave numbers in the x and y directions and $h(x,y)$ is the surface height. Our 512×256 height

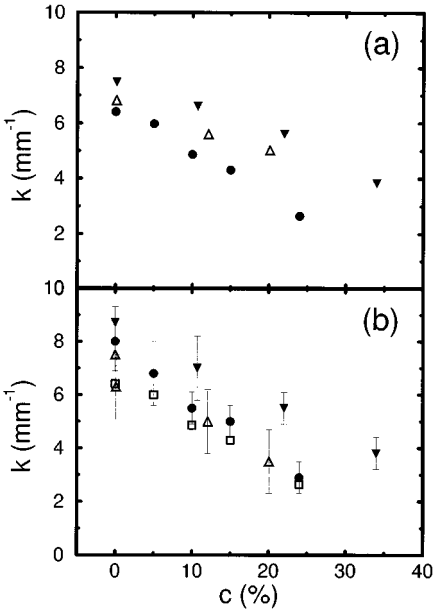

FIG. 7. k vs c for KBr (▼), NaCl (●), and KCl (△) determined from (a) video micrographs and (b) Fourier transform. Micrograph data for NaCl (□) are included in (b) for comparison.

data were split into two 256×256 segments and a 2D fast Fourier transform was performed on each. The resulting two power spectra were averaged together. $S(\vec{k})$ was azimuthally averaged to get the power per unit k, $P(k)$, using

$$P(k)=\int_0^{2\pi} S(\vec{k})k\,d\theta, \qquad (10)$$

where $k=\sqrt{k_x^2+k_y^2}$. The power spectra $P(k)$ for NaCl surface patterns at five different concentrations are plotted in

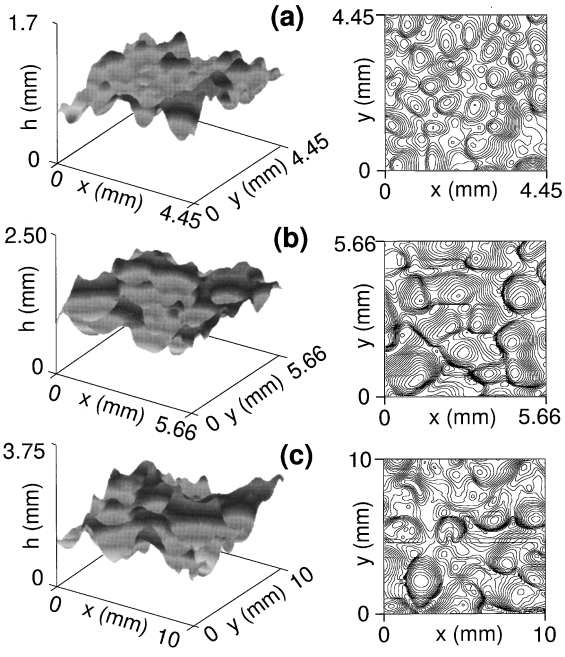

FIG. 8. Gray-scale-coded profile plots (left) and corresponding contour plots (right) for NaCl dissolved in aqueous solutions of NaCl with (a) $c=0\%$, (b) $c=15\%$, and (c) $c=24\%$.

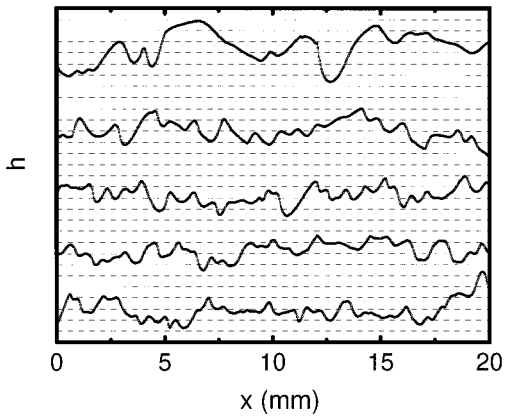

FIG. 9. Linear surface profiles for NaCl surfaces exposed to aqueous solutions of five different concentrations of NaCl in ascending order: $c=0\%$, 5%, 10%, 15%, and 24%. The distance between dashed lines corresponds to 0.15 mm.

Fig. 10. The power spectra show a broad distribution of wave-lengths with a ''shoulder'' that signals a rapid falloff in power at higher wave number. This shoulder moves to lower wave number at higher solution concentrations consistent with our visual analysis of the video micrographs. The breadth of the power spectrum makes it difficult to determine the wave number corresponding to this shoulder. Although the raw power indicates a broad wave-number distribution, at least some of this is a result of overall slant or curvature in the crystal when it is measured. For example, the power spectrum of a flat plane inclined with respect to a plane perpendicular to the profilometer tip is proportional to $1/k^2$. The degree to which this is a real consequence of dissolution or merely an artifact of the measurement is not known. In any case it distorts the power spectra appreciably. To correct for this distortion we tried a background subtraction of a plane and also one with quadratic curvature. This improved the spectra, but not completely. In practice, we found that scaling the power by k^2 worked the best. Some examples of this procedure are shown in Fig. 11, where we plot

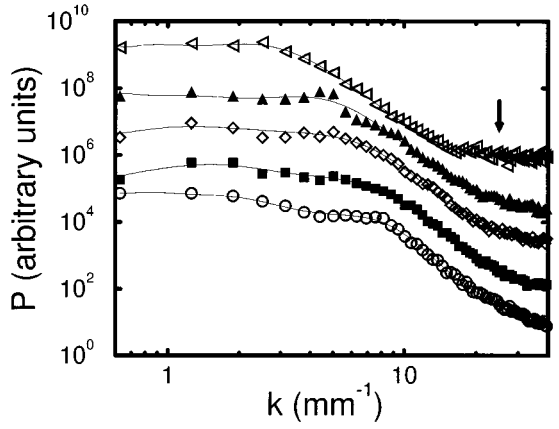

FIG. 10. Power spectra for NaCl surface patterns at different concentrations $c=0\%$ (○), 5% (■), 10% (◇), 15% (▲), and 24% (◁). For clarity, each spectrum has been shifted vertically by a factor of 10 relative to the previous spectrum in order of increasing concentration. The arrow indicates an upper cutoff wave number set by the diameter of the profilometer tip.

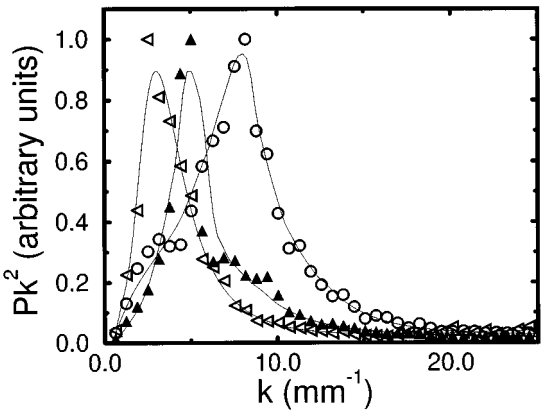

FIG. 11. Power spectra multiplied by k^2 and then normalized so that peaks are of unit magnitude, for NaCl dissolved in solutions with $c=0\%$ (○), 15% (▲), and 24% (◁). The lines are guides to the eye.

$P'(k)\equiv k^2P(k)$ normalized so that $P'(k_{\max})=1$. The peak of each curve is chosen as the characteristic wave number associated with the surface pattern. The characteristic wave numbers determined from the above method are plotted in Fig. 7(b) against the solution concentration. Also shown are data from the micrograph method for NaCl. We see that there is quite close agreement between the two methods.

V. DISCUSSION

Figure 12 plots δ/δ_0 as a function of $\Delta\rho/\rho$ on logarithmic scales. This is a test of the scaling relation of the marginal stability hypothesis as expressed by Eq. (6). Visually, we see that the data are consistent with a $-\frac{1}{3}$ scaling relation. Fitting the data to the form $\delta/\delta_0=[R_c/(\Delta\rho/\rho)]^{1/3}$, we find that for NaCl, $R_c=88$, for KBr, $R_c=66$, and for KCl, $R_c=75$. These values are roughly an order of magnitude smaller than one would expect from a literal interpretation of Howard's original hypothesis. The marginal stability hypothesis is seen, however, to be useful in correlating the dissolution rate data. For a more sensitive test, we fit the data to the form $\delta/\delta_0=[R_c/(\Delta\rho/\rho)]^x$. The results are given in Table IV. Power-law scalings are observed over about a decade in $\Delta\rho/\rho$ with exponents consistent with either $\frac{1}{3}$ or $\frac{2}{7}$.

It is interesting to speculate on whether a more precise

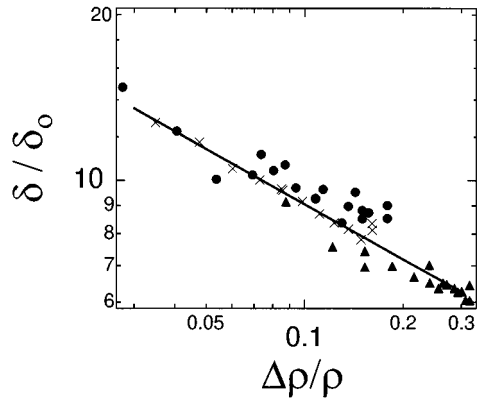

FIG. 12. δ/δ_0 vs $\Delta\rho/\rho$ for NaCl (●), KBr (▲), and KCl (×). The slope of the solid line is $-\frac{1}{3}$.

TABLE IV. Values of x and R_c from fits to δ/δ_0 vs $\Delta\rho/\rho$. Ranges of δ and δ/δ_0 used in the fit are also shown.

Salt	x	R_c	δ (mm)	$\Delta\rho/\rho$
NaCl	-0.29 ± 0.05	133 ± 26	0.054–0.077	0.041–0.18
KBr	-0.26 ± 0.06	100 ± 18	0.038–0.052	0.088–0.32
KCl	-0.34 ± 0.04	75 ± 15	0.046–0.086	0.034–0.16

experiment would have revealed $\frac{1}{3}$ or $\frac{2}{7}$ scaling. It is not obvious from the thermal convection results that one would expect $\frac{2}{7}$ in this case. First, the crossover Rayleigh number for observation of nonclassical scaling is predicted to increase with Prandtl (or Schmidt) number [11] and our Schmidt numbers are much larger than the Prandtl numbers of the thermal experiments. Second, the morphological deformation of the interface may change the stabilization properties of the shear flow. Third, the thermal experiments have a heated bottom plate and a cooled top plate. This leads to the interaction of two turbulent boundary layers, one on each plate. The dissolution experiments are more closely analogous to a single heated plate in an infinite fluid container. Nonclassical scaling has not been demonstrated in this situation for the thermal problem.

We now turn to a comparison of the lateral length scales with the prediction of Foster's linear stability analysis. Figure 13 plots the dimensionless wave number k/k_0 of the surface patterns as a function of $\Delta\rho/\rho$ where $k_0 \equiv (g\Delta\rho/D\nu\rho)^{1/3}$. The prediction of Foster's analysis, Eq. (7), gives $k/k_0 = 0.123$, which is shown in Fig. 13. We see that scaling of the surface pattern is consistent with Foster's linear theory for the most unstable wave number and only differs from Foster's prediction by a constant factor of about 2. This agreement is quite remarkable considering the fact that the actual process is quite far from onset, involves a moving, deformable solid boundary, and that the different salt solutions have quite different fluid parameters. This scaling relation is strong evidence that the surface patterning is determined by the turbulent fluid motion.

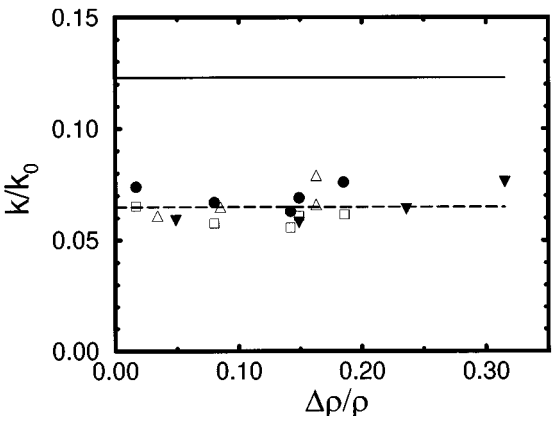

FIG. 13. k/k_0 vs $\Delta\rho/\rho$ for NaCl (●,□), KCl (△), and KBr (▼). The dashed line is the average value of the data and the solid line is the theoretical prediction.

VI. CONCLUSION

We have presented data on the rates of dissolution of NaCl, KBr, and KCl in aqueous solution of the respective salts. We find that the dissolution rate is controlled by turbulent fluid convection in the solution. The dissolution rate is well predicted by a turbulent boundary layer model adapted from work on thermal convection. The turbulent convection produces a pattern on the solid-liquid interface that has not previously been characterized systematically. We find that the linear stability analysis of Foster [36] predicts the scaling properties of the lateral length scale and (to within a factor of 2) the length scale itself.

This system remains very rich. Better calculations are called for to obtain a more quantitative understanding of the mass transport and surface pattern length scales. More precise experiments are needed to check for the possibility of nonclassical scaling of mass transport in the system. The time evolution of the interface looks very interesting. Some potentially important time scales are the diffusion time (δ^2/D), a diffusion front time ($0.6\delta^2/D$, Ref. [36]), and a Rayleight-Taylor time ($0.1\delta^2/D$, Ref. [39]). Roughly an order of magnitude separates the largest and smallest estimates for the evolution times and quantitative measurements may help further elucidate the pattern formation mechanism. More work is also needed to establish how the pattern amplitude varies with time. Does it reach a steady state? Does the wave number stay constant in time? It will also be interesting to test these ideas in related systems to test whether they are of general validity.

ACKNOWLEDGMENTS

We would like to acknowledge Jim Steele for his observations and support that initiated this project. We thank L. Kramers, Helmut Brand, Ning Li, and Yuchou Hu for helpful remarks. William J. Brown IV and Michael D. Kerkel (Kenyon College) helped acquire some of the data presented in this paper. This work was funded by the U.S. Department of Energy and by Kenyon College.

[1] C. Shin and D. Economou, Int. J. Heat Mass Transfer **33**, 2191 (1990).
[2] T. Sukegawa, M. Kimura, and A. Tanaka, J. Cryst. Growth **92**, 46 (1988).
[3] M. Small and I. Crossley, J. Cryst. Growth **27**, 35 (1974).
[4] S. Coriell, J. Cryst. Growth **49**, 13 (1980).
[5] D. Hurle, E. Jakeman, and A. Wheeler, J. Cryst. Growth **58**, 163 (1982).
[6] M. Glicksman, S. Coriell, and G. McFadden, Annu. Rev. Fluid Mech. **18**, 307 (1986).

[7] S. Forth and A. Wheeler, J. Fluid Mech. **236**, 61 (1992).
[8] F. Heslot, B. Castaing, and A. Libchaber, Phys. Rev. A **36**, 5870 (1987).
[9] B. Castaing, G. Gunaratne, F. Heslot, L. Kadanoff, A. Libchaber, S. Thomae, X.-Z. Wu, S. Zaleski, and G. Zanetti, J. Fluid Mech. **204**, 1 (1989).
[10] M. Sano, X. Z. Wu, and A. Libchaber, Phys. Rev. A **40**, 6421 (1989).
[11] B. I. Shraiman and E. Siggia, Phys. Rev. A **42**, 3650 (1990).
[12] I. Procaccia, E. Ching, P. Constantin, L. Kadanoff, A. Libchaber, and X.-Z. Wu, Phys. Rev. A **44**, 8091 (1991).
[13] B. Gluckman, H. Willaime, and J. Gollub, Phys. Fluids A **5**, 647 (1993).
[14] J. Werne, Phys. Rev. E **48**, 1020 (1993).
[15] For example, see Y. Jaluria, *Natural Convection Heat and Mass Transfer* (Pergamon, Oxford, 1980).
[16] R. Goldstein, E. Sparrow, and D. Jones, Int. J. Heat Mass Transfer **16**, 1025 (1973).
[17] R. Kerr, J. Fluid Mech. **280**, 287 (1994).
[18] D. Fang and A. Hellawell, J. Cryst. Growth **92**, 364 (1988).
[19] I. Campbell, Econ. Geol. **81**, 1118 (1986).
[20] R. Kerr, J. Fluid Mech. **280**, 255 (1994).
[21] For a review, see M. Epstein and F. B. Cheung, *Annu. Rev. Fluid Mech.* **15**, 293 (1983).
[22] S. Davis, U. Müller, and C. Dietsche, J. Fluid Mech. **144**, 133 (1984).
[23] L. Hadji, M. Schell, and D. Riahi, Phys. Rev. A **41**, 863 (1990).
[24] J. Pantaloni, M. Velarde, R. Bailleux, and E. Guyon, C. R. Acad. Sci. Paris B **285**, 275 (1977).
[25] Y. Yen, Phys. Fluids **11**, 1263 (1968).
[26] Y. Yen, J. Heat Transfer **102**, 550 (1980).
[27] R. Farhadieh and J. L. Baker, J. Heat Transfer **100**, 305 (1978).
[28] K. Taghavi-Tafreshi, V. Dhir, and I. Catton, J. Heat Transfer **101**, 318 (1979).
[29] R. Farhadieh and M. Epstein, J. Heat Transfer **104**, 199 (1982).
[30] J. Selman and C. Tobias, Adv. Chem. Eng. **10**, 211 (1978).
[31] A. Wragg, Electrochim. Acta **13**, 2159 (1968).
[32] A. Wragg and R. Loomba, Int. J. Heat Mass Transfer **13**, 439 (1970).
[33] L. Howard, in *Applied Mechanics*, Proceedings of the 11th International Congress of Applied Mechanics, Munich, 1966, edited by H. Gortler (Springer, Berlin, 1966), p. 1109.
[34] W. Malkus, Proc. R. Soc. London Ser. A **225**, 196 (1954).
[35] C. Priestly, *Turbulent Transfer in the Lower Atmosphere* (University of Chicago Press, Chicago, 1959).
[36] T. Foster, J. Geophys. Res. **73**, 1933 (1968).
[37] Though not relevant to the experiments reported here, we note that if the solute thermal diffusivity is small compared to the mass diffusivity and there is a significant latent heat associated with the dissolution, then the rate of dissolution may be controlled by thermal rather than mass diffusion. If, in addition, the thermal diffusivity of the solid is larger than the thermal diffusivity of the liquid, then the dissolving interface can be unstable to a morphological instability similar to the Mullins-Sekerka instability [52]. This can be seen by considering a perturbation of a flat interface that protrudes into the liquid. Heat flow to the protuberance will be reduced by the reduced thermal gradient in the region. This reduces the rate of dissolution of the protuberance relative to the surrounding portion of the interface and hence causes the protuberance to grow.
[38] J. Lommel and B. Chalmers, Trans. Met. Soc. AIME **215**, 499 (1959).
[39] S. Chandrasekhar, *Hydrodynamic and Hydromagnetic Stability* (Oxford University Press, Oxford, 1961).
[40] X.-Z. Wu and A. Libchaber, Phys. Rev. A **43**, 2833 (1991).
[41] T. Foster, Geophys. Fluid Dyn. **2**, 201 (1971).
[42] Bicron Tech., Solon, OH 44139.
[43] Melles Griot Inc., Models 11 NCS 001 and 11 NCM 001.
[44] RDT Electronics Inc, Model D5-100H.
[45] A. Lo Surdo, E. Alzola, and F. Millero, J. Chem. Thermodyn. **14**, 253 (1982).
[46] W. Linke, *Solubilities, Inorganic and Metal Organic Compounds*, 4th ed. (Van Nostrand, Princeton, 1958), Vol. 2.
[47] *The Handbook of Chemistry and Physics*, edited by R. Weast (Chemical Rubber Company, Boca Raton, FL, 1981).
[48] N. Vargaftik, *Tables on the Handbook of Physical Properties of Liquids and Gases*, 2nd ed. (Hemisphere, Washington, DC, 1983).
[49] *American Institute of Physics Handbook*, 3rd ed., edited by D. Gray (McGraw-Hill, New York, 1972).
[50] R. Stokes and R. Mills, *Viscosity of Electrolytes and Related Properties* (Pergamon, New York, 1965).
[51] J. Kestin, H. Khalifa, and R. Correia, J. Phys. Chem. Ref. Data **10**, 57 (1981).
[52] W. W. Mullins and R. Sekerka, J. Appl. Phys. **34**, 323 (1963).